Natural Convection in Trenches of High Aspect Ratio

R. H. Nilson[z] and S. K. Griffiths

Sandia National Laboratories, Livermore, California 94551-0969, USA

Filling deep trench-like features by electrodeposition is often limited by ion transport from the electrolyte bath to the plating surface at the feature bottom. This transport may be substantially enhanced by buoyancy-driven convection induced by metal-ion depletion adjacent to the plating surface. Numerical solutions of the Navier-Stokes and species transport equations are used to determine the magnitude of transport enhancement, expressed as a Sherwood number, for Rayleigh numbers ranging from 10^3 to 10^8 and for feature aspect ratios of depth to width ranging from 1 to 16 both for open trenches and for fully enclosed rectangular domains. To facilitate extrapolation of these numerical results, an exact analytical solution is derived for aspect ratios much greater than unity. This is used in conjunction with the known asymptotic behavior for large Rayleigh numbers to construct a composite formula relating the Sherwood number to the Rayleigh number and aspect ratio. The results indicate that buoyancy-driven convection may provide significant transport enhancement during electrodeposition into features having depths greater than about 100 μm and that enhancement exceeding a factor of ten may occur in LIGA features having depths of 1 mm or more. It is also shown that a moderate inclination of the substrate helps to suppress the formation of multiple vertically stacked convective cells that would otherwise reduce the overall transport.
© 2003 The Electrochemical Society. [DOI: 10.1149/1.1569480] All rights reserved.

Electrodeposition into microscopic trenches is of importance in damascene plating of interconnects for semiconductor devices[1] and in the LIGA process[2,3] used to produce metal parts having feature sizes ranging from micrometers to millimeters. In LIGA, a high-energy X-ray source is used to expose a thick photoresist through a patterned mask. The exposed material is then removed by chemical dissolution to obtain a nonconducting mold having a metallic substrate. The mold cavities are then filled by electrodeposition. The resulting metal parts may be the final product or may be used as injection or embossing molds for mass production.

Deposition rates in recessed features are often limited by transport of metal ions into the feature, particularly in LIGA applications where feature depths typically range from 100 micrometers to more than a millimeter. If the electrolyte within these features is stagnant, the minimum required diffusion-limited plating times range from about 2 to 20 days for 1-3 mm feature depths. Pumping of electrolyte over the mold top provides effective transport into features having aspect ratios, A = depth/width, less than about two but provides little benefit in features having higher aspect ratios. This is because the convective cell that circulates the fluid in the top of each feature penetrates only about one feature width. Additional counter-rotating convective cells are formed deeper within high aspect ratio features, but the circulation speeds in successive cells decrease by nearly two orders of magnitude.[4] Thus, prior studies addressing the influence of forced convection on etching[5-7] and electrodeposition[8-11] in microscopic trenches have either reaffirmed this expectation or have been limited to aspect ratios near unity.

Unlike forced convection driven by flow over the mold top, buoyancy-driven convection may strongly enhance the transport in high-aspect-ratio features, particularly for feature depths of 1 mm or more. Removal of metal ions from the electrolyte reduces the local fluid density at the plating surface by as much as 10% when plating at relatively high rates from 1 M nickel baths. Because of its reduced density, the depleted electrolyte rises from an upward-facing electrode, permitting the inflow of fresh electrolyte. In an earlier study[12] it was postulated that this mechanism was responsible for measured current densities 10 to 100-fold in excess of the diffusion-limited current. That study also included some numerical calculations that demonstrated the importance of buoyancy in the LIGA application.

Despite the relatively large density differences associated with ion depletion, there is relatively little mention of buoyancy-driven natural convection in the electroplating literature. This is because natural convection plays only a secondary role in conventional plating of flat surfaces when the fresh electrolyte is supplied to the plating surface by vigorous stirring of the bath. However, in the absence of such stirring, buoyant convection can strongly enhance plating rates on flat surfaces[13] and on long upward-facing tracks.[14] It has also been demonstrated both experimentally and computationally[15] that natural convection is important in the shape-evolution of electrodeposits in rectangular cavities of unit aspect ratio provided that the depth of the feature is greater than about 100 μm. In LIGA the feature depth is usually at least this large and aspect ratios range from less than unity to ten or more.

Beyond the literature of electrodeposition and microfabrication there are hundreds of studies of natural convection induced by gradients of temperature and chemical composition,[16,17] but few of these deal directly with the configuration of interest here. Previous studies addressing convection in tall slender domains are mainly concerned with transport induced by gradients of temperature and density orthogonal to the gravity field as in the pioneering studies by Elder[18] and Gill[19] and in a recent paper[20] on multicellular convection at very high aspect ratios. Conversely, previous studies exploring motion driven by density gradients parallel to the gravity field (our current interest) have largely focused on relatively shallow layers, as in the classical Rayleigh-Benard problem that is posed on a heated plane of infinite width.[17,21] Notable exceptions to these general observations include studies of Rayleigh-Benard convection in honeycomb structures[22] for $0.5 < A < 2.5$ and in rectangular boxes[23] for $1 < A < 4$. However, the regime of primary interest for LIGA, that of very high aspect ratios, remains largely unexplored.

To better understand the role of natural convection in electroplating of deep recesses, we have performed a series of numerical simulations for $1 < A < 16$ and Rayleigh numbers ranging from 10^3 to 10^8. The results indicate that natural convection can provide a substantial increase in ion transport into LIGA molds having depths of 100 μm or more, but the occurrence of multicellular convection at high Rayleigh numbers may reduce this benefit. However, it is further shown that tilting of the substrate can help to maintain a favorable unicellular flow structure. These numerical results are used to guide the development of a physically based analytical model that can be readily used to calculate mass-transport rates in trenches for $A > 1$ and for all Rayleigh numbers.

Governing Equations

We consider the simplified geometry of a single trench-like cavity of width w and instantaneous height h as shown in Fig. 1. Since the time required for mold filling is large compared to the relaxation time of the flow and transport fields, the filling process is nearly

[z] E-mail: rhnilso@sandia.gov
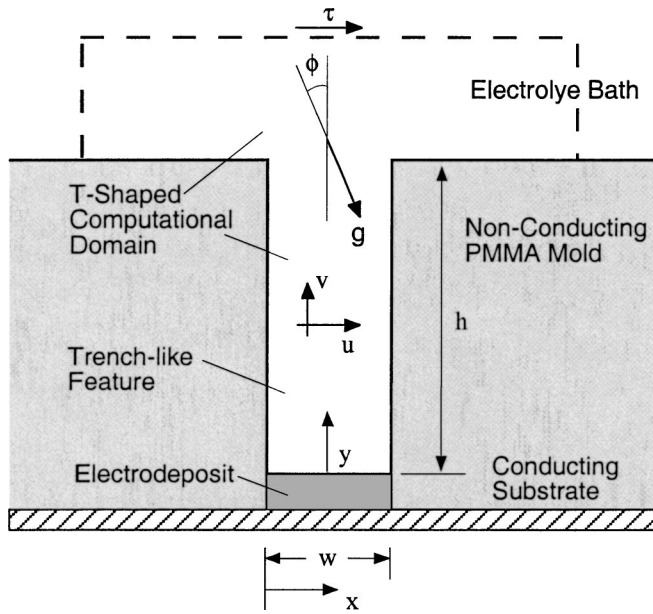
Figure 1. Schematic of a trench-like cavity in a nonconducting mold. Metal ions are carried from the mold top to the deposition surface at the trench bottom by convection and diffusion.

quasi-steady and the plating surface motion has little effect on the fluid velocity field. Further, we assume that the plating surface remains flat, since observed lateral variations are generally small compared to the feature height, particularly when aspect ratios are large. Far above the mold top, $y \gg h$, species concentrations are assumed uniform at values typical of the plating bath. To isolate the effects of buoyancy, we restrict attention to transport by convection and diffusion with the understanding that ion drift induced by the electric field may sometimes be important.[11] For simplicity, we focus attention on the transport and surface deposition of a single metal ion species that is largely responsible for the fluid density variations that drive convective motion.

Under these idealizations, the equations describing conservation of mass for a nearly incompressible fluid may be written[24]

$$\nabla \cdot \mathbf{u} = 0 \qquad [1]$$

$$\frac{\partial C}{\partial t} + \nabla \cdot (\mathbf{u}C) = \nabla \cdot (D\nabla C) \qquad [2]$$

where $\mathbf{u} = u\mathbf{i} + v\mathbf{j}$ is the fluid velocity vector, C is the partial molar density of the deposition species, and D is the effective binary diffusivity for that species.

Under the customary Boussinesq approximation, the fluid density is treated as though it were uniform except in evaluating the buoyancy force, $\rho\mathbf{g}$, appearing in the following statement of momentum conservation[25-27]

$$\rho \frac{\partial \mathbf{u}}{\partial t} + \rho(\mathbf{u} \cdot \nabla \mathbf{u}) = -\nabla p + \rho \mathbf{g} + \mu \nabla^2 \mathbf{u} \qquad [3]$$

Here, p is the pressure and the dynamic viscosity, μ, is presumed uniform. The density variations that drive the motion can be related to ion concentrations by a linear approximation of the form

$$\rho = \rho_0 + \Delta\rho \left(\frac{C - C_0}{C_0} \right) \qquad [4]$$

in which C_0 and ρ_0 are the bath concentration and density, and $\Delta\rho$ is the density reduction that results from full depletion of the plating species.

To facilitate numerical solution by finite difference methods, it is convenient to rewrite the governing equations for two-dimensional flow in terms of the normalized stream function ψ^* and vorticity ω^*.[25-27] The stream function is defined in a manner that ensures satisfaction of the continuity equation

$$u^* = \frac{\partial \psi^*}{\partial y^*} \quad \text{and} \quad v^* = -\frac{\partial \psi^*}{\partial x^*} \qquad [5]$$

Here, the position coordinates, time, and velocity components are respectively scaled by the feature height, h, and a reference velocity, D/h

$$x^* = \frac{x}{h}, \quad y^* = \frac{y}{h}, \quad t^* = \frac{tD}{h^2} \quad u^* = \frac{uh}{D}, \quad v^* = \frac{vh}{D},$$

$$\psi^* = \frac{\psi}{D}, \quad \omega^* = \frac{\omega h^2}{D} \qquad [6]$$

In terms of these scaled variables and a normalized metal ion concentration, $C^* = C/C_0$, the species conservation equation, Eq. 2, becomes

$$\frac{\partial C^*}{\partial t^*} + u^* \frac{\partial C^*}{\partial x^*} + v^* \frac{\partial C^*}{\partial y^*} = \frac{\partial^2 C^*}{\partial x^{*2}} + \frac{\partial^2 C^*}{\partial y^{*2}} \qquad [7]$$

Further, by cross differentiation and summation of the x and y components of the momentum equation, the pressure is eliminated from the following expression of momentum conservation

$$\frac{1}{Sc}\left(\frac{\partial \omega^*}{\partial t^*} + u^* \frac{\partial \omega^*}{\partial x^*} + v^* \frac{\partial \omega^*}{\partial y^*} \right) = -Ra\left(\frac{\partial C^*}{\partial x^*} + \frac{\partial C^*}{\partial y^*} \tan\phi \right)$$

$$+ \frac{\partial^2 \omega^*}{\partial x^{*2}} + \frac{\partial^2 \omega^*}{\partial y^{*2}} \qquad [8]$$

in which the normalized vorticity, ω^*, is defined in terms of velocity gradients

$$\omega^* = \frac{\partial v^*}{\partial x^*} - \frac{\partial u^*}{\partial y^*} \qquad [9]$$

Note that the buoyancy forces driving convective motion now appear as spatial derivatives of the metal ion concentration, C^*, and that ϕ is the inclination angle of the y axis, measured from the vertical. Finally, the stream function and vorticity are related through the equation

$$\omega^* = -\left(\frac{\partial^2 \psi^*}{\partial x^{*2}} + \frac{\partial^2 \psi^*}{\partial y^{*2}} \right) \qquad [10]$$

as readily verified by substituting Eq. 5 into Eq. 9. This last elliptic equation is used to calculate the stream function from values of the vorticity.

The two parameters appearing in the momentum equation are the Rayleigh and Schmidt numbers; both are written in terms of the kinematic viscosity $\nu = \mu/\rho_0$

$$Ra \equiv \frac{\Delta\rho g_y h^3}{\rho_0 D\nu} \quad \text{and} \quad Sc \equiv \frac{\nu}{D} \qquad [11]$$

The Rayleigh number is based on the magnitude of the gravity force component acting downward along the trench axis, $g_y = g \cos\phi$, as this is the primary driving force for feature scale circulation. Since the Schmidt number is typically of the order 10^3 for small ions in an aqueous solution, the time derivative and the advective vorticity transport on the left side of Eq. 8 are generally negligible. In this asymptotic regime, there is essentially no dependence of the solutions on the Schmidt number. The only remaining parameter is the

Rayleigh number, a measure of the strength of the buoyancy-driven motion. For LIGA features having depths, h, ranging from 0.1 to 10 mm the Rayleigh number is on the order of 10^3-10^9. This estimate is based on a relative density difference of $\Delta\rho/\rho_0 = 0.1$, as appropriate for a 1 M nickel bath and full depletion of metal ions at the deposition surface. The actual value of the normalized surface concentration is, however, controlled by the boundary condition at the plating surface.

Numerical Approach

The preceding partial differential equations are solved numerically on the T-shaped domain shown in Fig. 1. The lower rectangular part of the domain represents a trench-like cavity of height h and width w. Since the sidewalls of the trench are electrical insulators, plating occurs on the floor alone. The wider region above the trench represents a portion of the plating bath. Although this bath is actually much larger than the trench, only a small portion need be included in the computational domain, provided that the boundary conditions are judiciously chosen. To reduce sensitivity of the solution to the location of these boundaries, the flow is permitted to pass through them as freely as possible. When the local velocity on these surfaces carries fluid into the domain, the normalized concentration is set to unity, as appropriate for the inflow of fresh electrolyte. Conversely, for an outward flow, boundary values of the concentration are extrapolated from the interior of the domain along the local flow direction. Similarly, values of the stream function are extrapolated from the interior to satisfy invariance of the stream function along the flow path. These extrapolations ensure that the gradients of C^* and ψ^* are orthogonal to $\mathbf{u}^*$

$$\mathbf{u}^* \cdot \nabla \psi^* = 0 \quad \text{and} \quad C^* = 1 \quad \text{or} \quad \mathbf{u}^* \cdot \nabla C^* = 0 \quad [12]$$

These free streaming boundary conditions are appropriate when the fluid above the mold is driven only by natural convection. Stirring or pumping of the electrolyte may be modeled, however, by applying an external shear stress, τ, along the top surface of the T-shaped domain[12]

$$\frac{\partial^2 \psi^*}{\partial y^{*2}} = \frac{\partial u^*}{\partial y^*} = \frac{\tau h^2}{\mu D} = \tau^* \quad [13]$$

This boundary condition replaces the extrapolation of the stream function from the interior to the top boundary in one of the upcoming example calculations.

The T-shaped computational domain shown in Fig. 1 is typically extended four trench widths above the trench mouth and two trench widths to each side of the trench. For external domains this large or larger, the transport within deep trenches becomes nearly insensitive to the domain size because most of the transport resistance resides within the feature itself rather than within the external domain. This holds true even though the structure of the buoyancy-driven motion above the feature may be quite sensitive to the domain size and applied boundary conditions. Despite these external variations, the flow within the trench remains unaltered because the free streaming boundary conditions in Eq. 12 allow the ambient high-density fluid to flow freely through any of the domain boundaries and into the trench mouth. Similarly, the ion-depleted fluid leaving the trench flows outward without impediment through any of the domain boundaries above the trench. This open-loop flow in and out of the trench may be disrupted, however, by forced flow over the top of the trench, because this may cause closure of the streamlines within the trench, reducing the ion transport into the trench, as seen in the example calculations. In these cases having external flow over the feature mouth, consistent results are obtained as long as the computational domain is extened one or more trench widths above the feature, provided that the external flow is driven by an applied shear stress rather than a prescribed external fluid velocity.

All the impermeable solid boundaries, both within the feature and external to it, may be viewed as one continuous streamline on which

$$\psi^* = 0 \quad \text{and} \quad \frac{\partial C^*}{\partial \eta^*} = 0 \quad [14]$$

where η^* is in a direction normal to each surface. The first of these strictly applies at all mold boundaries, and it should also provide an excellent approximation on the deposition surface since the translational speed of this boundary is generally much smaller than the characteristic fluid speed. The second applies everywhere except on the deposition surface at the mold bottom. In addition, both of the velocity components are zero on all solid surfaces (ignoring the slight translational speed of the plating surface), and these conditions are reflected in the boundary values of vorticity that are calculated from the defining equation, Eq. 9.

Rather than incorporating any specific electrode kinetics we have chosen to apply more generic boundary conditions that allow us to isolate the effects of buoyancy-driven transport

$$\frac{\partial C^*}{\partial y^*} = K^* C^* \quad \text{or} \quad C^* = 0 \quad \text{on} \quad y^* = 0 \quad [15]$$

The first of these relates the diffusion flux to a surface deposition rate proportional to the local ion concentration. For large values of the normalized rate constant, K^*, the surface concentration is nearly zero over the entire lower surface, corresponding to the maximum deposition rate.[12] Thus, for the present purpose of computing the vertical transport it is simpler to require that $C^* = 0$, as we do in all the upcoming examples. Moreover, since the ion concentration at the feature bottom influences only the vertical density difference appearing in the Rayleigh number, these solutions are equally applicable to cases having any nonzero, but relatively uniform, ion concentration at the feature bottom. The neglected variations in ion concentration across the feature bottom are of importance in controlling the evolving shape of the deposition surface but have only a secondary influence on the overall transport along the feature, particluarly when the aspect ratio is large.

Our goal is to compute the buoyancy-driven transport as a function of the Rayleigh number based on the vertical concentration difference. Thus, the principal result of each calculation is the Sherwood number, Sh, representing the ratio of the total vertical transport by convection and diffusion to that which would occur by diffusion alone

$$Sh = \left(\frac{h}{D\Delta C}\right)\frac{1}{w}\int_0^w \left(D\frac{\partial C}{\partial y} - vC\right)dx \quad [16]$$

This integral is the same at all elevations in a steady flow. The normalization is based on the concentration difference over the feature height, ΔC, representing the difference between the areal average across the feature mouth and the prescribed zero concentration at the mold bottom. This ensures that $Sh \to 1$ when there is no fluid motion within the trench. When the transport is strong or the aspect ratio is large, the concentration difference along the feature and the overall difference between the bath and the feature bottom are nearly the same. Note, however, that the Rayleigh number is always based on the overall density difference between the bath and the feature bottom.

The equations are solved numerically on a square mesh. Derivative operators are replaced by finite difference approximations to obtain a system of algebraic equations for the time evolution of the nodal point values of all dependent variables. At each time step the iterative solution procedure includes several steps:[25-27] (*i*) use Eq. 7 to explicitly compute new values of C_{ij}^*; (*ii*) use derivatives of the new concentration field in solving Eq. 8 for new values of ω_{ij}^*; (*iii*) use the new vorticity field in solving Eq. 10 for ψ_{ij}^*; (*iv*) differen-

tiate the new stream function to calculate velocity components from Eq. 5; and (v) differentiate the velocity field to calculate boundary values of vorticity from Eq. 9.

The time step for the concentration field is chosen so that the relative and absolute changes at any nodal point do not exceed prescribed limits. Because the Schmidt number is asymptotically large, hundreds or even thousands of much smaller time steps must be taken to advance the vorticity transport equation to the same time level. In essence, the vorticity and stream function equations are relaxed to a steady state for each change in the concentration field. Thus, since we are mainly interested in steady-state solutions, it is more efficient to compute a false transient wherein the vorticity and stream function are only partially relaxed for each update of the concentration field. The two methods generally yield the same results for steady flows but may differ for oscillatory or chaotic motions, because the false transient alters the influence of Schmidt number on transient behavior. To speed the calculations and to test convergence, each problem is converged to a steady or quasi-steady state on successively finer meshes having 11, 21, 41, 81, and in some cases 161 nodal points across the trench. Since the mesh is square, the number of nodal points along the trench axis is larger in proportion to the aspect ratio.

Results for Fully Enclosed Rectangular Domains

Although our primary interest is in transport within rectangular domains that are open at the top, we first review some example calculations for flow in fully enclosed rectangular cavities. This provides an opportunity for model validation by comparison with previous calculations and experimental results. Although these comparisons address thermally induced convection, the governing equations are analogous to those for convection induced by variations in ion concentration. The only differences are that the normalized temperature, T^*, replaces the normalized ion concentration, C^*, the thermal diffusivity replaces the binary diffusion coefficient, D, and the Rayleigh number in Eq. 11 is based the thermally induced density variation $\Delta\rho = \alpha\Delta T$ where α is the thermal expansion coefficient and ΔT is the overall temperature difference. We began by computing the flow and transport in a square enclosure having an imposed temperature difference between the vertical sidewalls, as in the Elder-Gill problem. Each of the sidewalls is isothermal while the top and bottom surfaces are insulated. Our results for mean transport rates agree with previous numerical calculations[27,28] within 5% for $A = 1$ and $10^3 < Ra < 10^5$ as well as for $A = 4$, $Ra = 2 \times 10^5$, and various inclination angles.

Experimental data was also used for model validation. Figure 2 illustrates the good agreement between our numerical results for the Rayleigh-Benard problem and published data from several sources that are included in Ref. 17, 29, and 30. Recall that in the Rayleigh-Benard configuration the horizontal top and bottom surfaces are isothermal, with the bottom at a higher temperature, and the sidewalls are insulated. The data sets shown in Fig. 2 are quite consistent even though they include aspect ratios ranging from $A \ll 1$ to $A = 1$. The results are relatively insensitive to the aspect ratio because the convective motion in layers much wider than their depth naturally evolves into a multicellular structure of counter-rotating cells each having an aspect ratio near unity.

The lines in Fig. 2 indicate our numerical results for $A = 1$ and for inclination angles of 0 and 25°. For each case, the time mean Sherwood number is shown by a solid line and a pair of dotted lines are used show the maximum and minimum values of the Sherwood number for the last 20,000 time steps of simulations that were each run for a total of 50,000 time steps. For $Ra < 10^5$ the minimum and maximum are nearly identical to the mean because the flow is essentially steady. However, at higher Rayleigh numbers the flow becomes quasi-steady, eventually causing a factor of two or greater spread between the maximum and minimum.

In the absence of substrate tilting ($\phi = 0$), the gravity field is parallel to the density gradient as in the classical Rayleigh-Benard
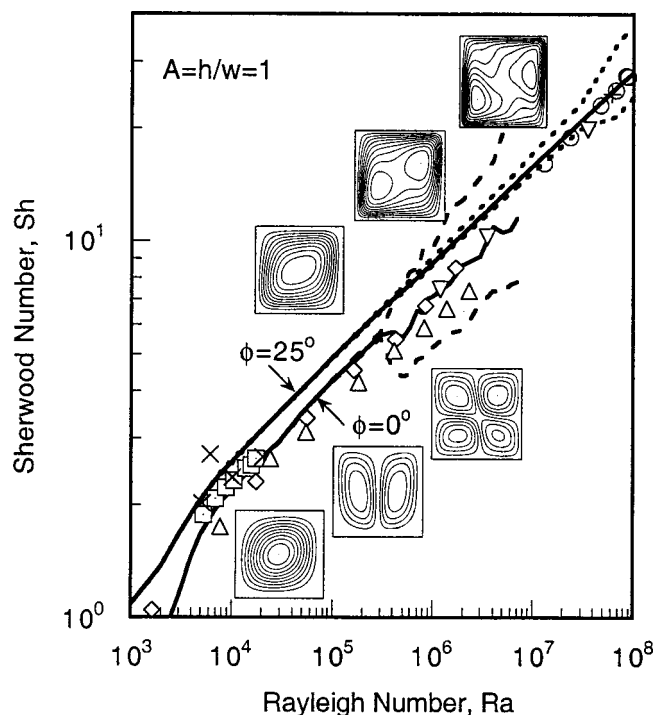

Figure 2. Comparison of experimental data for Rayleigh-Benard convection (symbols) with numerical calculations (lines) for a square enclosure tilted at angles, ϕ, of 0 and 25° from vertical. Insets show computed streamline patterns. (——) Time-averaged results; (· · · ·, — — —) instantaneous upper and lower bounds. (upper ——, · · · ·) for $\phi = 25$°; (lower ——, — — —) for $\phi = 0$°. All experimental data is for $\phi = 0$°.

problem. Under these conditions the fluid remains motionless and convective disturbances decay in time whenever the Rayleigh number is less than a critical value, Ra_{crit}. Above this threshold any disturbance will grow to a steady or quasi-steady buoyancy-driven flow. The stability analysis of Platten and Legros[17] yields critical Rayleigh numbers ranging from 1767 to 2585 for $0.2 \leq A \leq 1$. Our calculation for $\phi = 0$ puts the onset at about 2500, in good agreement with the stability analysis for $A = 1$. In our calculational approach, the initial ion concentration field is skewed to induce convective motion that dies out whenever $Ra < Ra_{crit}$.

Our numerical results for $\phi = 0$ are in relatively good agreement with the experimental data from the onset of convection up to a Rayleigh number of 4×10^5. Within this range, the computed streamline pattern changes substantially as indicated by the inset streamline plots for Rayleigh numbers of 10^4, 10^5, and 4×10^5. At small Ra the flow is unicellular, it then becomes bicellular, and finally transitions to a pattern with four cells. The Sherwood number drops abruptly at the transition from two to four cells, as readily apparent in the plot. Beyond this point the flow becomes oscillatory with qualitative changes in the flow pattern and large deviations between instantaneous values of the Sherwood number. The jagged variation of the time mean Sherwood number above $Ra = 4 \times 10^5$ is probably due to the limited duration of the averaging period. Aside from this, the calculations continue to follow the trend of the data quite well.

The upper set of lines and insets in Fig. 2 indicate calculational results for a square enclosure tilted 25° from the vertical. This relatively moderate inclination stabilizes the flow and yields relatively steady solutions for Rayleigh numbers approaching 10^8. As seen in the insets for Rayleigh numbers of 10^5, 10^6, and 10^7, the streamline pattern remains essentially unicellular over the full range, though secondary cells do form within the central core. The calculations
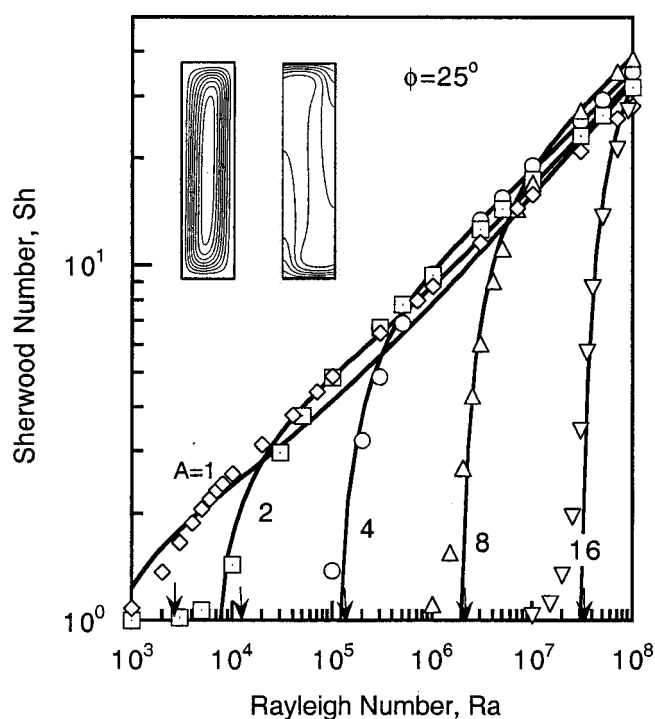
Figure 3. Comparison of numerically calculated Sherwood number (symbols) with analytical model (lines) for fully enclosed rectangular domains having aspect ratios $1 \leq A \leq 16$. Enclosures are tilted 25° from vertical. Inset shows streamlines (left) and isopleths (right) for $A = 4$ and $Ra = 10^6$.

Figure 4. Streamlines (left) and concentration contours (right) for $Ra = 10^6$ and $\phi = 25°$. Strong convective motion carries fresh electrolyte deep into feature, reducing the thickness of the diffusive boundary layer at the plating surface.

remain in relatively good agreement with the experimental data both for small and large Rayleigh numbers, with the greatest deviations seen in the intermediate range where there is considerable scatter in the data from various sources.

The calculations appear to correctly approach the experimentally observed asymptotic behavior wherein the Sherwood number is proportional to the third root of the Rayleigh number (see slope in Fig. 2), as discussed later in more detail. In general we were quite pleased to find this level of agreement, particularly for large Ra, since the one-third power asymptote is thought by some to apply only when the flow is highly turbulent. The experiments of Elder[31] suggest that the transition to turbulence occurs around $Ra \approx 10^9\text{-}10^{10}$, though the one-third power asymptote has been observed[30] to hold up to 10^{11}.

Tilting of the enclosure not only stabilizes the flow, it also alters the onset of convection in a qualitative manner. When a component of the gravity field is orthogonal to the initial density gradient, convective motion is induced for all values of the Rayleigh number as in the Elder-Gill configuration. However, as seen in Fig. 2, a 25° tilt produces a Sherwood number of only ~1.3 for a Rayleigh number of 2500. So the enhancement to purely diffusive transport is moderate at the threshold normally associated with the Rayleigh-Benard motion. With increasing aspect ratio, the enhancement due to Elder-Gill convection becomes even less significant relative to the much stronger Rayleigh-Benard convection, as seen in Fig. 3.

Figure 3 displays numerically computed Sherwood numbers (symbols) *vs.* Rayleigh number for an inclination angle of 25° and for $A = 1, 2, 4, 8$, and 16. The five solid lines are the results of an approximate analytical model derived in a later section of this paper. Since the enclosure is tilted, there is some enhancement or transport for all Rayleigh numbers. However, it is clear that the computed threshold for strong convection increases with the aspect ratio. Moreover, the computed variation of this threshold is in good agreement with the critical Rayleigh numbers predicted by the stability
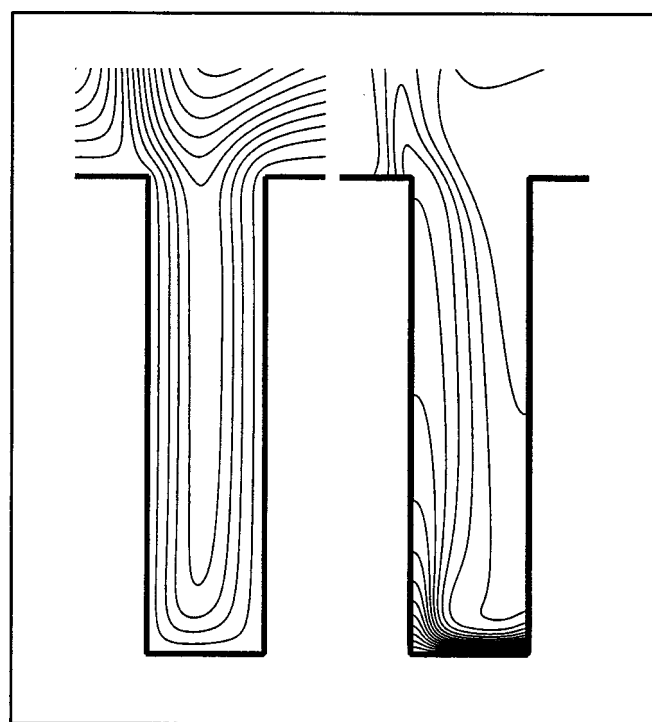
analysis of Platten and Legros[17] indicated by arrows at the base of the plot. Note that the stability limit for large aspect ratios increases as $Ra = 532\,A^4$ according to Platten and Legros.[17] The constant in this asymptotic expression is about a factor of two smaller than that derived in the well-known book by Chandrasekhar.[21] The smaller, more accurate value is obtained by use of more general expressions for the presumed spatial dependence of the disturbance.

Although no experimental data appears in Fig. 3, its is seen that all of the calculations for fully enclosed domains approach a third-root asymptote at high Rayleigh numbers and, as seen earlier in Fig. 2, this asymptote is in good agreement with measurements for $A \leq 1$. The experiments of Prasad and Koseff[23] also confirm this asymptote for aspect ratios of $1 \leq A \leq 4$. Moreover, the results of Catton and Edwards[22] for honeycomb cells approach a slightly shifted one-third power asymptote that applies for $0.5 \leq A \leq 2.5$. Thus, both the available data and the present numerical calculations suggest that the upper asymptote does not depend strongly, if at all, on the aspect ratio. However, in the next section of this paper it is shown that this asymptote is shifted by a factor of two between fully enclosed rectangular domains and open trenches.

Typical streamlines and isopleths, lines of constant ion concentration, are presented in the inset of Fig. 3 for $A = 4$, $Ra = 10^6$, and $\phi = 25°$. The flow is essentially parallel along the midsection. The turning regions at the top and bottom are almost identical and each occupies about one half channel width. With increasing aspect ratio, these turning regions remain nearly the same while the central parallel flow domain simply expands in length to fill the growing midsection. Although the streamline pattern is relatively insensitive to Ra, fluid speeds increase with increasing Rayleigh number. In response, the ion concentration boundary layers on the top and bottom surfaces become thinner with increasing Rayleigh number and the ion concentration along the midsection becomes progressively more uniform. Many of these features are shared by buoyancy-driven flow in trench-like domains.
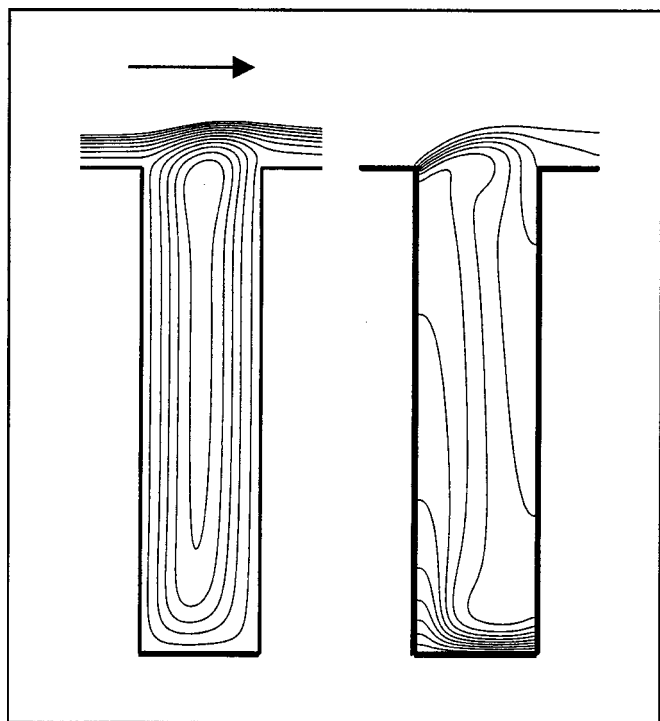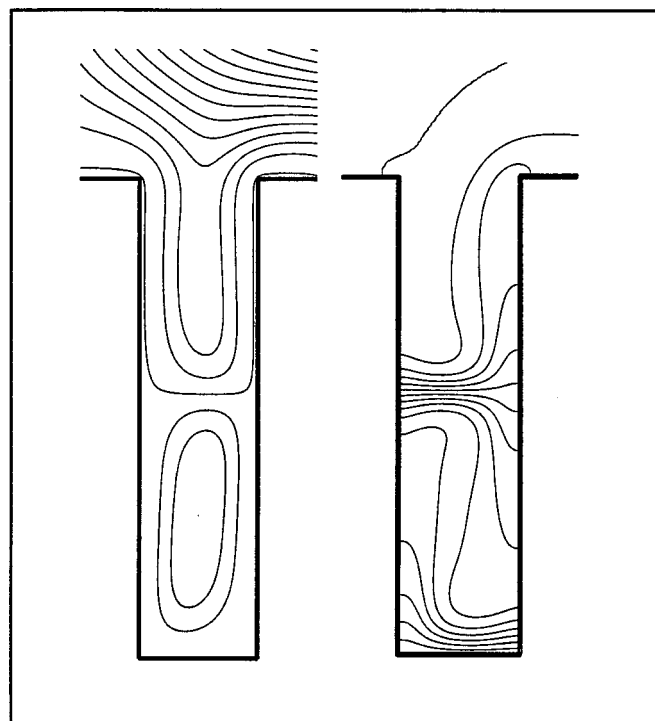
Figure 5. Streamlines (left) and concentration contours (right) for $Ra = 10^6$, $\phi = 25°$, and a normalized shear stress of $\tau^* = 10^4$ above mold. Flow over the mold top may close convective streamlines and reduce transport.

Figure 6. Streamlines (left) and concentration contours (right) for bicellular convection in a vertical trench for $Ra = 10^6$, $\phi = 0$, and $\tau^* = 0$. Transport is inhibited by the presence of a diffusion layer at midheight where ion species are exchanged between the two counter-rotating cells.

Results for Open Trenches

Figure 4 presents streamlines and isopleths for flow in an open trench with an aspect ratio of four and a Rayleigh number of 10^6. The 25° inclination angle of the feature is apparent since the rising low-density fluid turns toward the vertical direction as it exits the left side of the trench.

The isopleths of Fig. 4 reveal a narrow boundary layer just above the plating surface at the trench bottom. In this region the fluid motion is essentially parallel to the bottom, requiring that the surface-normal flux be carried by diffusion alone. The local axial gradient must thus be steeper here than in the upper region where the flux is carried advectively by opposing axial streams having differing ion concentrations. These side-to-side differences in concentration are apparent in the nearly axial, rather than transverse, orientation of the isopleths at midheight. As the descending fluid approaches the plating surface, it compresses the isopleths on the right side, whereas the ascending fluid expands the isopleths on the left. This asymmetry of motion produces a lateral variation in the axial ion flux and corresponding deposition rate that may alter the shape of the electrodeposit as illustrated by simulations of the shape evolution.[9,11,15,32] The ion flux to the plating surface of Fig. 4 corresponds to a Sherwood number of about 14. This 14-fold enhancement is consistent with the concentration field, because the steep gradients are now confined to only about 10% of the feature depth. Ion concentrations just above that layer are nearly equal to the bath concentration, shortening the diffusion distance by a factor of ten.

The primary difference between transport in open and closed domains is well illustrated by a comparison of the isopleths in Fig. 4 with those shown in the inset of Fig. 3. These two cases share the same Rayleigh number and so have comparable fluid speeds. In both figures, the isopleths have the same equal increments of concentration. In both, the isopleths are widely spaced along the midsection of the trench where the axial transport is dominated by advection. Thus, most of the transport resistance is localized within the thin boundary layers at the bottoms of both trenches and at the top of the enclosed trench. Since the resistance of each layer is inversely proportional to its thickness and the layers are of comparable thickness, it follows that the overall transport resistance is only half as great when there is one boundary layer rather than two. Thus, the ion flux and the Sherwood number for the open trench are about twice as large as those of the fully enclosed trench. This factor of two benefit may be disrupted, however, by an external flow over the mold surface or by the occurrence of multiple convection cells.

Contrary to intuition, a strong external flow over the top surface of a plating mold may inadvertently decrease the transport of ion species into the open features. This is illustrated in Fig. 5 where an external shear stress of $\tau^* = 10^4$ is applied to the upper surface of the tee-shaped domain. This normalized shear is equivalent to that produced by a mean flow speed of 60 mm/s in a channel of height 20 mm above a mold having a depth of 1 mm. The Rayleigh number is maintained at 10^6, as in Fig. 4. With the flow coming from the left and a tilt angle of 25° clockwise, the external flow streams across the top of the mold, rather than descending into the open trench. The convective cell becomes a closed loop driven by shear forces as well as buoyancy. Despite the increase in fluid circulation speed, the overall transport is reduced because a new diffusion layer must form at the top of the trench to transfer ions from the external flow into the circulation loop. In contrast, a somewhat weaker shear force would have still permitted open loop circulation. Moreover, an external flow of the same magnitude from the opposite direction would descend into the trench and return to the main stream without closing the circulation loop. Thus, to maximize transport, the direction of the external flow should be upward along an inclined mold face. This orientation reinforces the buoyancy-driven circulation that draws the fresh high-density electrolyte inward along the lower trench wall.

The formation of multiple vertically stacked convection cells may also substantially reduce transport along open trenches or fully enclosed domains. For example, the bicellular pattern visible in the
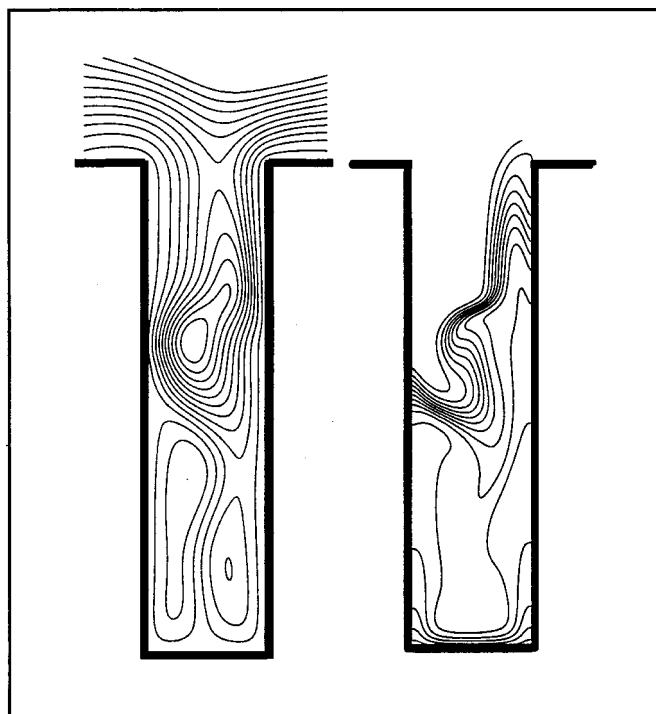
Figure 7. Instantaneous streamlines (left) and isopleths (right) for an oscillatory flow in a vertical trench for $Ra = 10^7$, $\phi = 0$, and $\tau^* = 0$. Flow is not truly steady, but instead wanders among several multicellular patterns.

Figure 8. Ion concentration varies linearly with height over the midsection of high-aspect-ratio trenches and enclosures for Rayleigh numbers only moderately exceeding the critical Rayleigh number. Concentration profiles and inset streamlines (left) and isopleths (right) are for $Ra = 2 \times 10^5$.

streamlines on the left side of Fig. 6 has the same Rayleigh number as the open convection loop of Fig. 4. In fact, the bicellular structure appears to be the preferred steady-state solution for a vertical trench. The single open loop is favored, however, when the axis of the feature is inclined by 25° as in Fig. 4. In that tilted orientation, the component of gravity acting across the feature pulls the heavier fluid toward the lower sidewall. Thus, tilting reduces the tendency toward a bicellular pattern in which the opposite rotation of the cells necessarily places the heavier fluid on opposite walls in the upper and lower cells. Our calculations suggest that a tilt of 25° is sufficient to maintain open-loop circulation in features having aspect ratios $1 \leq A \leq 8$ for Rayleigh numbers up to 10^8.

Multicellular flows are generally less efficient than single-cell structures in transporting ion species. Although the preceding three examples all have the same Rayleigh number, the Sherwood number decreases by more than a factor of two between the single open-loop configuration of Fig. 4 and the closed-loop single and multicellular structures of Fig. 5 and 6. The primary reason for this is apparent in the ion concentration fields on the right sides of Fig. 4 and 6. Although both configurations have boundary layers at the deposition surface, only the bicellular flow has an additional diffusion layer at midheight. Here, steep concentration gradients are needed for diffusion exchange of ionic species between the upper and lower cells. Advection cannot enhance this exchange since no flow crosses between the two cells. The presence of two diffusion layers, rather than one, reduces the Sherwood number by roughly a factor of two. In addition, the presence of multiple cells generally reduces horizontal density differences, leading to slower fluid speeds and weaker transport. This same reasoning applies equally well to Fig. 5 where flow over the feature top produced a closed cell having two diffusion layers rather than one.

The diversity and complexity of flow patterns increases with Rayleigh number, and the flow is increasingly likely to wander between two or more alternative patterns.[31,33] These observations are illustrated by the instantaneous flow field shown in Fig. 7. Here, the trench is vertical and Rayleigh number is 10^7, ten times greater than
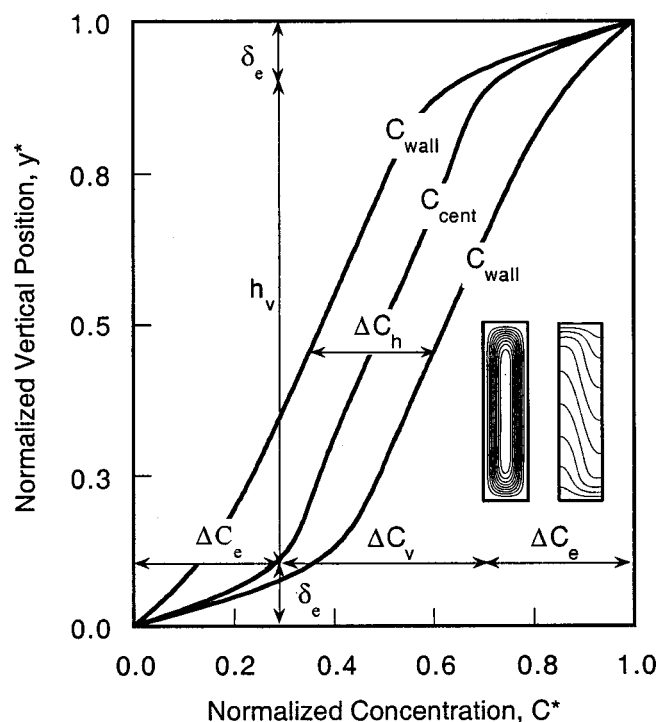
in the preceding examples. The flow field shown in Fig. 7 consists of three cells, two of them side by side. In other instantaneous flow patterns these side-by-side cells are sometimes nearly symmetric about the vertical center line of the feature and occasionally extend over most of the height. At other times one cell dominatse as the other shrinks into a corner. Occasionally, one of the lower cells becomes pinched at the waist and splits vertically in half. Similar, but less complex oscillations were also seen in our inital example of flow in a rectangular box. Open trenches with larger aspect ratios are simply able to accommodate a greater diversity of alternative flow structures.

Despite all this chaotic motion, the time average of the Sherwood number converges to a relatively stable mean on time scales that are still much shorter than typical electrodeposition times. The time-averaged Sherwood number for the flow of Fig. 7 is about 17, though instantaneous values range from about 10 to 24. However, when the trench is inclined by 25°, the same Rayleigh number produces a single open cell having a Sherwood number of about 40. A plot of the computed Sherwood number as a function of Rayleigh number and aspect ratio for open trenches is presented after first deriving an analytical model that yields the same information.

An Exact Solution for Large Aspect Ratios

At moderate Rayleigh numbers, ion concentrations vary linearly with elevation along the midsection of high-aspect-ratio features. This linearity is apparent in Fig. 8 which displays the axial variation of the concentration on each of the sidewalls and the center line of a vertical enclosure for $A = 4$ and $Ra = 2 \times 10^5$. There are boundary layers at the top and bottom; there would be one such layer at the bottom of an open trench. It is also seen in preceding streamline plots and in the inset of Fig. 8 that the flow is usually parallel to the feature walls along the midsection such that the transverse velocity component becomes negligible. This zone of parallel flow and linear concentration is obviously greater for higher aspect ratios and so occupies a large portion of the height.[24]

Based on these observations the governing equations, Eq. 2 and 3, may be reduced to the following pair describing steady-state species and momentum conservation for flow and transport along the midsection of high-aspect-ratio trenches

$$v\frac{\partial C}{\partial y} \approx v\frac{\Delta C_v}{h_v} = D\frac{\partial^2 C}{\partial x^2} \qquad [17]$$

$$\rho g + \frac{\partial p}{\partial y} \approx (\rho - \rho_o)g = \mu\frac{\partial^2 v}{\partial x^2} \qquad [18]$$

Here, ρ_o is the mean density at any height of interest. Note that the deletion of $\partial^2 C/\partial y^2$ from Eq. 17 does not imply that vertical diffusion is unimportant but rather that the gradient is uniform. For convenience we introduce the following definition of the normalized ion concentration, a normalized lateral coordinate measured from one trench wall, and a new notation for the vertical concentration gradient

$$\hat{C} = \frac{C - C_o}{\Delta C_h} = \frac{\rho - \rho_o}{\Delta \rho_h}, \quad \hat{x} = \frac{x}{w}, \quad \frac{\partial C}{\partial y} = \frac{\Delta C_v}{h_v} \quad [19]$$

The symbols ΔC_h and $\Delta\rho_h$ indicate the lateral or horizontal differences in density and concentration across the trench, while ΔC_v is the vertical concentration difference over the central linear region of height h_v.

After insertion of these definitions, the resulting expression for the vertical velocity from Eq. 17 is substituted into Eq. 18 to obtain the following fourth-order ordinary differential equation for the normalized ion concentration

$$\lambda\hat{C} = \frac{d^4\hat{C}}{d\hat{x}^4} \qquad [20]$$

The parameter λ appearing here is proportional to the vertical density gradient, $\Delta\rho_v/h_v$, and the fourth power of the trench width

$$\lambda \equiv \frac{\Delta\rho_v}{h_v}\frac{g_y w^4}{\mu D} \quad \text{where} \quad \Delta\rho_v = \Delta\rho_h\frac{\Delta C_v}{\Delta C_h} \qquad [21]$$

Note that λ may also be written in terms of a modified Rayleigh number, $\hat{R}a$, and a modified aspect ratio, $\hat{A}$

$$\lambda = \frac{\hat{R}a}{\hat{A}^4} \quad \hat{R}a \equiv \frac{\Delta\rho_v g_y h_v^3}{D\mu} \quad \hat{A} \equiv \frac{h_v}{w} \qquad [22]$$

Here $\hat{R}a$ and $\hat{A}$ are based on the vertical height, h_v, and vertical density difference, $\Delta\rho_v$, over the midsection of the trench where the concentration profile is linear.

A total of six boundary conditions must be satisfied on the trench sidewalls

$$\frac{d\hat{C}}{d\hat{x}} = \frac{d^2\hat{C}}{d\hat{x}^2} = 0 \quad \text{and} \quad \hat{C} = -\frac{1}{2} \quad \text{at} \quad \hat{x} = 0 \qquad [23]$$

$$\frac{d\hat{C}}{d\hat{x}} = \frac{d^2\hat{C}}{d\hat{x}^2} = 0 \quad \text{and} \quad \hat{C} = +\frac{1}{2} \quad \text{at} \quad \hat{x} = 1 \qquad [24]$$

The first derivative of $\hat{C}$ must vanish on each wall to prevent any diffusion into the walls. Also, in view of Eq. 17, the second derivative of $\hat{C}$ must vanish on each wall to ensure that the local vertical velocity (tangential to the wall) is zero, in accordance with the standard no-slip boundary condition of fluid mechanics. By analytical integration of Eq. 20 it can be further seen that the vanishing derivatives of $\hat{C}$ ensure that there is no net vertical mass flux through any horizontal cross section, as required to satisfy mass conservation

in a steady flow. Given the symmetry of these derivative boundary conditions, we make the symmetric choices of $\hat{C}(0) = -1/2$ and $\hat{C}(1) = +1/2$ to satisfy the requirements that $\hat{C}$ have a zero mean and an overall variation of unity consistent with the definition given in Eq. 19.

The problem might appear to be overconstrained since the differential equation is only of fourth order and a total of six boundary conditions must be satisfied on the trench sidewalls. However, the following analytical solution meets all these conditions for one specific choice of the parameter $\lambda = \hat{R}a/\hat{A}^4$

$$\hat{C} = -\frac{1}{4}\{\cos(\lambda^{1/4}\hat{x}) + \cosh(\lambda^{1/4}\hat{x}) - B[\sin(\lambda^{1/4}\hat{x})$$
$$- \sinh(\lambda^{1/4}\hat{x})]\} \qquad [25]$$

where

$$B = -\frac{\sin(\lambda^{1/4}) - \sinh(\lambda^{1/4})}{\cos(\lambda^{1/4}) - \cosh(\lambda^{1/4})} \qquad [26]$$

The numerical value of the eigenvalue, λ, is determined by the following characteristic equation

$$\cos(\lambda^{1/4})\cosh(\lambda^{1/4}) = 1 \qquad [27]$$

having the root

$$\lambda = \frac{\hat{R}a_{crit}}{\hat{A}^4} = 500.563917 \qquad [28]$$

Thus, the corresponding critical value of the Rayleigh number increases with the fourth power of the aspect ratio, $\hat{R}a_{crit} \approx 500\hat{A}^4$.

At the onset of convection the convective motion is so weak that it cannot appreciably alter the vertical concentration gradient and hence $dC/dy = \Delta C/h = \Delta C_v/h_v$ is the same at all elevations. It follows from Eq. 11, 21, and 22 that, at this juncture, $Ra/A^4 = \hat{R}a/\hat{A}^4$ and hence

$$Ra_{crit} = \lambda A^4 \approx 500A^4 \qquad [29]$$

Quite remarkably, the critical Rayleigh number deduced from these steady-state considerations is nearly the same as the asymptotic stability limit of $Ra_{crit} = 535A^4$ derived by Platten and Legros[17] based on the growth and decay of perturbations to a motionless state in a high-aspect-ratio trench.

Figure 9 illustrates the good agreement between the preceding exact solution (solid lines) and results (symbols) obtained by numerical solution of the full equations. The values of $\hat{C}$ and $\hat{v}$ for the numerical solutions were computed from the definition of $\hat{C}$ given in Eq. 19 and the following definition of $\hat{v}$

$$\hat{v} = v\frac{\Delta C_v}{h_v}\frac{w^2}{D\Delta C_h} = v\frac{\lambda\mu}{gw^2\Delta\rho_h} = \frac{d^2\hat{C}}{d\hat{x}^2} \qquad [30]$$

using the nodal point values of C and v, wall-to-wall values of ΔC_h, and central-difference values of $\Delta C_v/h_v = dC/dy$ that applied at the specific vertical heights of interest. The symbols shown in Fig. 9 are mostly taken from midheight profiles, though numerical results are included for quarter height and three-quarter height locations for $A = 8$. Note that the selected Rayleigh numbers are only moderately greater than Ra_{crit} for each of the three aspect ratios, as apparent from the corresponding values of the Sherwood number, $Sh = 1.44$, 3.21, and 6.05 for aspect ratios of 2, 4, and 8. In general, the exact solution remains valid for higher Sherwood numbers when the aspect ratio is larger.
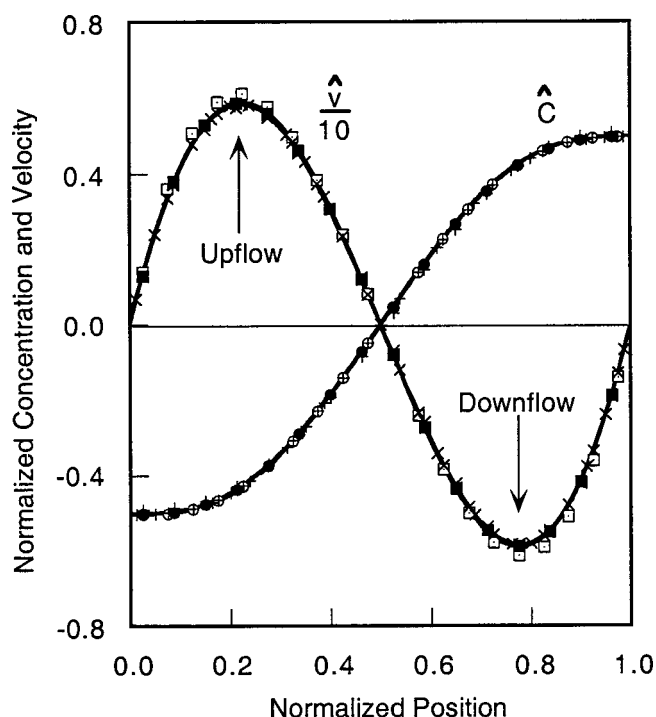
Figure 9. Comparison of exact solutions (solid lines) with numerical calculations (symbols). Open symbols for $A = 2$, $Ra = 10^4$, $Sh = 1.44$, and $y^* = 1/2$. Filled symbols for $A = 4$, $Ra = 2 \times 10^5$, $Sh = 3.21$, $y^* = 1/2$. Plus and cross symbols for $A = 8$, $Ra = 3 \times 10^6$, $Sh = 6.05$, $y^* = 1/4, 1/2, 3/4$.

It might appear contradictory that an exact solution that supposedly exists for only one critical value of the parameter $\lambda = \hat{R}a/\hat{A}^4$ appears to apply over a range of Rayleigh numbers. However, the definition of $\hat{R}a$ is based upon the vertical concentration gradient, $\Delta C_v/h_v$, within the central zone of parallel flow. In contrast, the conventional Rayleigh number, Ra, is based on the overall height, h, and overall concentration difference ΔC. From the definitions of λ and Ra we may write

$$\lambda = \frac{Ra}{A^4} \frac{\Delta C_v}{\Delta C} \frac{h}{h_v} \quad \text{or} \quad \Delta C_v = \Delta C \lambda \frac{A^4}{Ra} \frac{h_v}{h} \qquad [31]$$

Further, using Eq. 28 to eliminate λ in favor of Ra_{crit}, it is seen that

$$\Delta C_v = \Delta C \frac{h_v}{h} \frac{Ra_{crit}}{Ra} \quad \text{for} \quad Ra > Ra_{crit} \qquad [32]$$

This relationship requires that the concentration difference and the gradient in the central region must both decrease with increasing Ra. To compensate for this, the gradient and the concentration difference in the end regions must increase with increasing Ra, as seen in the preceding numerical solutions.

Analytical Expression for the Sherwood Number

The Sherwood number representing the ratio of actual mass transfer to that which would have occurred by diffusion alone may be written

$$Sh = \frac{\Delta C_e}{\delta} \frac{h}{\Delta C} \qquad [33]$$

where ΔC_e is the difference in concentration across a diffusion layer of thickness δ at the trench bottom. In closed rectangular regions

there are at least two such diffusion layers, one at each end. Open trenches have at least one diffusion layer at the bottom but may also have a diffusion layer at the top, particularly if a strong external flow is present. Using the symbol N to denote the number of diffusion layers, each presumed to have a comparable thickness and concentration difference

$$h = h_v + N\delta \quad \text{and} \quad \Delta C = \Delta C_v + N\Delta C_e \qquad [34]$$

where h_v and ΔC_v refer to the central region of parallel flow. The latter of these relations may be used to rewrite the Sherwood number as follows in terms of ΔC_v rather than ΔC_e

$$Sh = \left(1 - \frac{\Delta C_v}{\Delta C}\right) \frac{h}{N\delta} \qquad [35]$$

Using Eq. 32, the ratio $\Delta C_v/\Delta C$ may be replaced in terms of Ra/Ra_{crit} to obtain

$$Sh = \left(1 - h_v^* \frac{Ra_{crit}}{Ra}\right) \frac{1}{N\delta^*} \qquad [36]$$

in which

$$\delta^* = \frac{\delta}{h} \quad \text{and} \quad h_v^* = \frac{h_v}{h} = 1 - N\delta^* \qquad [37]$$

An approximate expression for the diffusion layer thickness, δ^*, is now constructed from the asymptotic limits that apply for small and large values of the Rayleigh number. At the onset of motion, convection aids diffusion along the midsection of the trench. However, as apparent in many of the preceding streamline plots, there is very little vertical convection in the end regions where the flow direction turns from downflow to upflow. In these turning regions having a thickness of roughly $\delta_0 = w/2$, the vertical species flux is carried mainly by diffusion. With increasing Rayleigh number the diffusion layer becomes progressively thinner because its thickness is controlled by diffusion from the horizontal crossflow to the adjacent surface. Although it is possible to derive an approximate expression for the boundary layer thickness based on the circulation speed, it is easier and probably more accurate to extract this information from other sources.
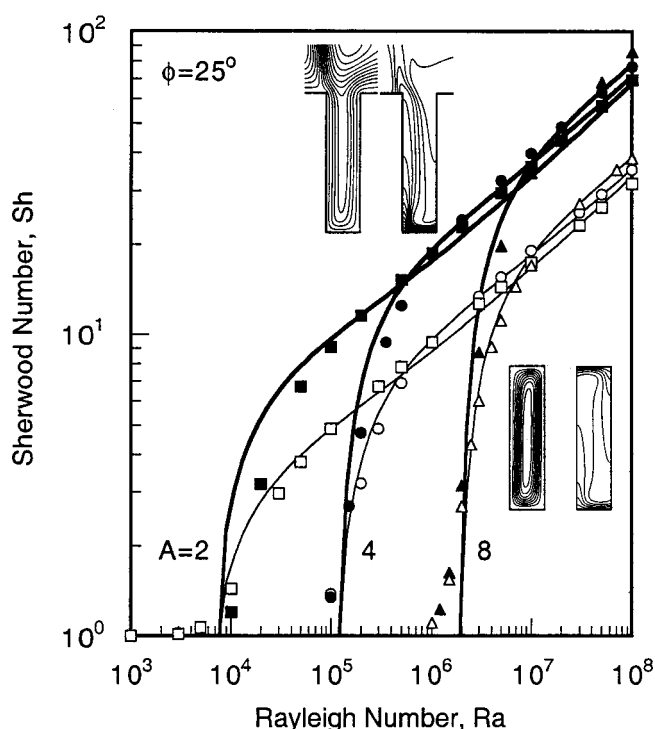
In the limit of high Rayleigh numbers we are guided by experimental studies,[29,30] scaling arguments,[33] and our numerical simulations which all suggest that $Sh \to \beta_{exp}Ra^{1/3}$. In this same limit $\Delta C_v/\Delta C \to 0$, $\Delta C_e/\Delta C \to 1/N$, and $h_v^* \to 1$. Thus, by equating the limit of our approximate expression for Sh, Eq. 36, with the empirical result it follows that

$$Sh \to \frac{1}{N_{exp}\delta_\infty^*} \approx \beta_{exp}Ra^{1/3} \quad \text{or} \quad \delta_\infty^* = \frac{1}{N_{exp}\beta_{exp}Ra^{1/3}} \qquad [38]$$

Goldstein and Tokuda[30] suggest a value of $\beta_{exp} = 0.0556$ based on experiments in closed containers, ($N_{exp} = 2$) at $Ra > 10^8$. Our numerical calculations for $N = 2$ suggest a somewhat larger value of $\beta_{exp} = 0.069$, perhaps because our Rayleigh numbers are smaller and the trench is slightly tilted. Thus, in the comparisons shown here we use $N_{exp}\beta_{exp} = 0.14$, about 20% above the Goldstein asymptote.

A composite expression for δ^* applicable for all Ra is constructed by simply forming the product of the preceding asymptotic expressions and dividing by their sum

$$\delta^* = \frac{\delta_0^* \delta_\infty^*}{\delta_0^* + \delta_\infty^*} \quad \text{where} \quad \delta_0^* = \frac{1}{2A} \quad \text{and} \quad \delta_\infty^* = \frac{1}{0.14Ra^{1/3}} \qquad [39]$$

Figure 10. Comparison of numerically computed Sherwood number (symbols) with analytical approximation (lines). Upper set of lines and filled symbols are for open trenches. Lower lines and open symbols for fully enclosed rectangular domains.

This formula correctly selects the smaller of the two asymptotes in both of the limits and provides a smooth transitional behavior at intermediate Rayleigh numbers.

Figure 10 illustrates the good agreement between the analytical approximation of Eq. 36 and 39 (solid lines) and our numerical calculations of the Sherwood number. The upper family of curves and data points is for open trenches ($N = 1$) while the lower family is for enclosed cavities ($N = 2$). The onset of convection is nearly the same for the two families, particularly when the aspect ratio is large. However, at large Rayleigh numbers, the transport in open trenches is a factor of two above that of the closed domains because there is one diffusion layer rather than two. In both families, the behavior for large Ra may ultimately be independent of the aspect ratio, though a slight offset still remains at $Ra = 10^8$. Although the analytical model was derived for a vertical trench, it appears to provide a good approximation to the numerical results for inclined enclosures provided that the Rayleigh number is based on the gravity force acting along the trench axis. This approach appears quite adequate for high aspect ratios, although it does shift the onset of convection somewhat, and it does not explicitly address the issue of stability against multicellular convection.

Applications

Diffusion-limited plating times for LIGA features are on the order of 2-20 days for 1-3 mm feature depths, assuming a bath concentration of 1 M/L. In addition to long process times, plating rates may be highly nonuniform in features having different aspect ratios, particularly if the electrolyte is pumped over the mold surface. Shallow features having aspect ratios of unity or less are well supplied by convective transport of plating ions, whereas high-aspect-ratio features are stagnant over most of their height.

Buoyancy-driven convection may substantially increase the transport into high-aspect-ratio features if the Rayleigh number is sufficiently large. Since the depletion of all metal ions from a 1 M nickel bath reduces the density by about 10%, the maximum Ray-

leigh number for features having depths of 0.1-10 mm ranges from 10^3 to 10^9 as computed from Eq. 11. Based on the stability criterion

$$Ra_{\text{crit}} \approx 500A^4 \qquad [40]$$

it follows that convection occurs for aspect ratios of $A < 1.2$, $A < 6.6$, and $A < 37$ for feature depths of 0.1, 1.0, and 10 mm, respectively. The same criterion implies that convection should be unimportant in trenches having a depth of less than 0.1 mm, consistent with previous experimental and numerical results for plating of bumps in cavitivies of unit aspect ratio.[15] Although the presumed feature geometry is trench-like, these results also serve as a guideline for electrodeposition into circular holes.

The preceding criterion and all of the foregoing calculations address fluid motions that are two-dimensional in a plane across the trench. If instead the fluid circulates in the long direction of a trench, the critical Rayleigh may be roughly approximated as

$$Ra_{\text{crit}} \approx 500A^2 \left(\frac{h}{L}\right)^2 \approx 500A^2 \qquad [41]$$

in which L is the trench length. This approximation is based on the observation that the fluid velocity for two-dimensional flow between closely spaced parallel walls may be written as

$$\mathbf{u} = -\frac{w^2}{12\mu}(\nabla p + \rho\mathbf{g}) \qquad [42]$$

where w is the wall spacing. This equation may be used to replace Eq. 18 in a scaling analysis of flow near the onset of convection to arrive at the very rough approximation given in Eq. 41. Nearly the same result can be found in stability analyses of thermal convection in Hele-Shaw cells[34] where the onset of convection occurs for a critical Rayleigh number of $48\pi^2 \approx 474$, which is fortuitously close to our approximate value of 500. This criterion would permit convection for aspect ratios, A, as large as 1.4, 44, and 137 for depths of 0.1, 1.0, and 10 mm, respectively, in trenches having length-to-depth ratios of unity. This result is roughly applicable to trenches much longer than their depth, since multiple side-by-side cells are then expected to form. For this reason we have taken h/L as unity in the final form of Eq. 44. The earlier, more restrictive criterion of Eq. 40 would still apply to holes and short trenches. Thus, the varying geometry of individual features in a given mold may cause order-of-magnitude differences in deposition rates, and in many cases deposition rates are subject to the diffusion limitations previously described. These nonuniformities could be avoided by plating with the trenches facing down, but only at the risk of trapping hydrogen bubbles within the trenches. Thus, a nearly horizontal inclination might provide the best configuration for suppression of convection.

If the Rayleigh number is large enough to produce strong convection in all features, the transport will be uniform for all feature widths and depths. This observation may be verified by substitution of the asymptotic expression for large Rayleigh numbers, $Sh \rightarrow 0.14Ra^{1/3}/N$, into the defining equation for the Sherwood number, Eq. 16.

$$q = ShD\frac{\Delta C}{h} = 0.14\Delta C \frac{D}{N}\left(\frac{\Delta\rho g}{\rho_0 D\nu}\right)^{1/3} \qquad [43]$$

Here, N is the number of convective boundary layers and q is the ion flux to the deposition surface. Since h disappears from the second of these equations, it follows that q is independent of the feature depth in a regime where this third root scaling holds. Under these circumstances, features of all depths and widths plate at the same rate, a condition of great potential benefit.

Summary

A numerical model has been developed and used to investigate enhancement of ion transport by natural convection during filling of trench-like cavities by electrodeposition. A finite difference procedure was used to solve the stream function and vorticity transport equations for fluid motion coupled with diffusive and convective transport of a metal ion species that is deposited at the trench bottom. Local depletion of that species adjacent to the plating surface induces the convective motion. The resulting enhancement of ion transport has been computed and reported in terms of a Sherwood number representing the ratio of transport by convection and diffusion relative to that which would have occurred by diffusion alone.

For purposes of validation, the model was first used to compute natural convection in fully enclosed square domains having imposed horizontal temperature differences. These results compared favorably with previous numerical calculations and experimental observations from several sources that collectively span Rayleigh numbers ranging from 10^3 to 10^8. At high Rayleigh numbers the computed Sherwood numbers increase with the third root of the Rayleigh number, in agreement with the experimental data. It was also seen that oscillatory multicellular motions may occur for Rayleigh numbers greater than about 10^5 but that these may be suppressed by a moderate inclination of the substrate.

Numerical results for ion transport into open trenches were presented for Rayleigh numbers ranging from 10^3 to 10^8 and for aspect ratios of height to width ranging from 1 to 16. Here again it was seen that oscillatory multicellular flows are likely to occur at higher Rayleigh numbers but that these could be suppressed by a 25° inclination of the substrate. Under this inclination, the heavier undepleted electrolyte flows into the trench along the lower sidewall and the ion-depleted fluid rises along the upper wall, providing a very effective open-loop circulation of the entire trench. However, it is further found that a strong flow over the mold top may produce a single closed-loop circulation cell that reduces the ion transport by about a factor of two relative to the open-loop configuration. This reduction results from the added transport resistance of an additional diffusion boundary layer at the trench mouth. Such closure of the open-loop circulation may sometimes be avoided by directing the external flow upward along the inclined mold face. However, an external flow velocity that is sufficient to maintain uniform ion concentrations across the mold face may also result in unwanted closed-loop circulation of recessed features.

This difference between open-loop and closed-loop circulation is also apparent in the roughly factor-of-two difference between the computed Sherwood numbers for open trenches and those for closed rectangular domains. The factor of two arises at high Rayleigh numbers because the transport resistance is localized within thin boundary layers that are present at both ends of a closed domain but only at the bottom end of an open trench under open-loop circulation. It is noted, however, that there is very little difference between open- and closed-loop configurations at or near the onset of convection, because both cases have similar frictional resistance when the aspect ratio is large.

A unique feature of the present work is the derivation of an exact analytical solution for convective transport in high aspect features at moderate Rayleigh numbers. Since the flow along the trench midsection is nearly parallel to the trench walls and the vertical concentration gradient is nearly linear, the governing equations can be reduced to a pair of second-order ordinary differential equations for the ion concentration and the axial velocity as functions of transverse position. The analytical solution to these equations entails an eigenvalue representing the critical Rayleigh number required to produce natural convection by a vertical density gradient in a high-aspect-ratio trench or enclosure. This threshold value of the Rayleigh number increases with the fourth power of the aspect ratio ($Ra_{\text{crit}} \approx 500A^4$), in good agreement with previous stability analyses based on presumed forms of the convective disturbance. The analytical solution is also in excellent agreement with our numerical solutions of the full equations.

Perhaps the most useful contribution of the present work is the formulation of an approximate analytical model that smoothly blends the preceding exact solutions that apply near the convection threshold with the complementary asymptotic solutions that apply for large Rayleigh numbers. This approximation provides relatively simple analytical formulas for the Sherwood number as a function of the Rayleigh number, aspect ratio, and the number of diffusive boundary layers for both trenches and for fully enclosed rectangular domains.

Although these results are applicable to convective flow in any rectangular cavity or trench, our principal interest is in filling of LIGA molds by electrodeposition. Here, the Rayleigh number for nickel plating from a 1 M bath ranges from about 10^3 to 10^9 for features having depths from 0.1-10 mm. Convective motions that are two-dimensional in a plane across the trench are expected to occur for aspect ratios of $A < 1.2$, $A < 6.6$, and $A < 37$ for feature depths of 0.1, 1.0, and 10 mm, respectively. Thus, for relatively thin LIGA photoresits (0.1 mm) convection is limited to features having aspect ratios less than $A = 1.2$, while at the deeper end of current practice (1.0 mm) convection occurs for aspect ratios less than $A = 6.6$. Buoyancy-driven convection will become more important as the LIGA fabrication technology is extended to feature depths greater than 1.0 mm. The analytical model derived here can be used to easily compute transport rates for any of these conditions and for other applications involving convective motions driven by variations in temperature and chemical composition.

References

1. *Electrochemical Processing in ULSI Fabrication I and Interconnect and Contact Metallization*, P. C. Andricacos, J. O. Dukovic, G. S. Mathad, G. M. Oleszek, H. S. Rathore, C. Reidsema-Simpson, D. D. Snyder, and R. K. Ulrich, Editors, PV 98-6, The Electrochemical Society Proceedings Series, Pennington, NJ (1998).
2. W. Ehrfeld and L. Lehr, *Radiat. Phys. Chem.*, **45(3)**, 349 (1995).
3. A. Maner, S. Harsch, and W. Ehrfeld, *Plat. Surf. Finish.*, **75(3)**, 60 (1988).
4. J. J. L. Higdon, *J. Fluid Mech.*, **159**, 195 (1985).
5. H. K. Kuiken, *Proc. R. Soc. London*, **A392**, 199 (1984).
6. M. Georgiadou and R. Alkire, *J. Electrochem. Soc.*, **141**, 675 (1994).
7. R. C. Alkire, H. Deligianni, and J. B. Ju, *J. Electrochem. Soc.*, **137**, 818 (1990).
8. K. G. Jordan and C. W. Tobias, *J. Electrochem. Soc.*, **138**, 1933 (1991).
9. K. Kondo and K. Fakui, *J. Electrochem. Soc.*, **145**, 3007 (1998).
10. K. M. Takahashi and M. E. Gross, *J. Electrochem. Soc.*, **146**, 4499 (1999).
11. M. Georgiadou, D. Veyret, R. L. Sani, and R. C. Alkire, *J. Electrochem. Soc.*, **148**, C54 (2001).
12. S. K. Griffiths, R. H. Nilson, A. Ting, R. W. Bradshaw, W. D. Bonivert, and J. M. Hruby, Report no. SAND98-8231, Sandia Nat. Lab., Feb 1998, summary appears in *Microsystem Technologies*, **4(2)**, 98 (1998).
13. I. Winkler, I. Plevan, and V. Nechiporuk, *Electrochim. Acta*, **41**, 2743 (1996).
14. C. Duchanoy, F. Lapicque, C. F. Oduoza, and A. A. Wragg, *Electrochim. Acta*, **46**, 433 (2000).
15. K. Hayashi, F. Fukui, Z. Tanaka, and K. Kondo, *J. Electrochem. Soc.*, **148**, C145 (2001).
16. B. J. Gebhart, Y. Jaluria, R. L. Mahajan, and B. Sammakia, *Bouyancy-Induced Flows and Transport*, Hemisphere, New York (1988).
17. J. K. Platten and J. C. Legros, *Convection in Liquids*, Springer-Verlag, New York (1984).
18. J. W. Elder, *J. Fluid Mech.*, **23**, 77 (1965).
19. A. E. Gill, *J. Fluid Mech.*, **26**, 515 (1966).
20. B. Lartigue, S. Lorente, and B. Bourret, *Int. J. Heat Mass Trans.*, **43**, 3157 (2000).
21. S. Chandrasekhar, *Hydrodynamic and Hydromagnetic Stability*, Clarendon Press, Oxford (1961).
22. I. Catton and D. K. Edwards, *J. Heat Transfer*, **89**, 295 (1967).
23. A. K. Prasad and J. R. Koseff, *Int. J. Heat Fluid Flow*, **17**, 460 (1996).
24. R. F. Probstein, *Physicochemical Hydrodynamics: An Introduction*, 2nd ed., John Wiley & Sons, Inc., New York (1994).

25. G. de Valh Davis, E. Leonardi, and M. P. van Schie, University of South Wales Report 1988/FMT/5 (June 1988).
26. J. N. Reddy and A. Satake, *J. Heat Transfer,* **102**, 659 (1980).
27. G. de Vahl Davis and I. P. Jones, *Int. J. Numer. Methods Fluids,* **3**, 227 (1983).
28. C. Y. Soong, P. Y. Tzeng, D. C. Chaing, and T. S. Sheu, *Int. J. Heat Mass Trans.,* **39**, 2869 (1996).
29. A. M. Garon and R. J. Goldstein, *Phys. Fluids,* **16**, 1818 (1973).
30. R. J. Goldstein and S. Tokuda, *Int. J. Heat Mass Trans.,* **23**, 738 (1980).
31. J. W. Elder, *J. Fluid Mech.,* **23**, 99 (1965).
32. G. H. Evans, K. S. Chen, R. S. Larson, and R. Greif, in *The 12th International Heat Transfer Conference*, Grenoble, France, August 18-23, 2002.
33. J. Patterson and J. Imberger, *J. Fluid Mech.,* **100**, 65 (1980).
34. J. S. Aniss, M. Souhar, and M. Belhaq, *Phys. Fluids,* **12**, 262 (2000).